Frequency-resolved measurement of two-color air plasma terahertz emission

Eiji Hase Institute of Post-LED Photonics, Tokushima University, 2-1 Minami-Josanjima, Tokushima 770-8506, Japan
hase@tokushima-u.ac.jp

Jérôme Degert CNRS LOMA, UMR 5798, Bordeaux University, Talence, France
jerome.degert@u-bordeaux.fr

Eric Freysz CNRS LOMA, UMR 5798, Bordeaux University, Talence, France
eric.freysz@u-bordeaux.fr

Takeshi Yasui Institute of Post-LED Photonics, Tokushima University, 2-1 Minami-Josanjima, Tokushima 770-8506, Japan
yasui.takeshi@tokushima-u.ac.jp

Emmanuel Abraham CNRS LOMA, UMR 5798, Bordeaux University, Talence, France
emmanuel.abraham@u-bordeaux.fr (corresponding author)

We investigated the far-field terahertz beam profile generated from an air plasma induced by two-color femtosecond laser pulses. Under our experimental conditions (filament length shorter than the dephasing length between the two-color pulses), using electro-optic sampling in both ZnTe (0.2-2.2 THz) and GaP (0.4-6.8 THz) crystals, and ultra-broadband ABCD technique (1-17.5 THz), we determined that the THz beam exhibits a unimodal beam pattern below 4 THz and a conical one above 6 THz. This experimental finding is consistent with theoretical studies based on the unidirectional pulse propagation equation, which predict the transition of THz emission from a flat-top profile to a conical one due to the destructive interference of THz waves emitted from the plasma filament. Our results also underscore the importance of accounting for experimental artifacts, such as photo-excited losses in silicon resulting in on-axis THz absorption along with the influence of drilled mirrors, in characterizing the complex spatial and frequency-dependent behavior of two-color plasma-induced terahertz emission.

Keywords: terahertz emission, two-color laser-induced plasma, air plasma filament, beam profile, electro-optic sampling, ABCD technique.

1 INTRODUCTION

Two-color laser-induced air plasma filaments are highly effective for generating intense (> 1 MV/cm) and ultrashort (sub-100 fs) terahertz (THz) pulses [1-4]. This so-called THz air photonics technique offers notable advantages, such as simplicity, self-repairing gas media, and the potential for high-intensity laser excitation. It also facilitates applications like ultra-broadband (> 20 THz) and nonlinear THz time-domain spectroscopy (THz-TDS) to probe THz-matter interactions from sub-THz to far-infrared frequencies. This experiment requires tight focusing, which is highly dependent on the spatial distribution of the THz radiation emitted from the air filament.

THz emission from a bichromatic air plasma has been explained by various models, including the two-dimensional (2D) transverse photocurrent or four-wave mixing, and can be numerically computed by

This provisional PDF is the accepted version. The article should be cited as: J. Eur. Opt. Society-Rapid Publ., https://doi.org/10.1051/jeos/2024042

the unidirectional pulse propagation equation [5-8]. Briefly, within the plasma filament produced by a focused femtosecond millijoule optical pulse at a fundamental frequency ω and its second harmonic 2ω, electrons undergo step-like acceleration, resulting in a frequency spectrum much broader than that supported by the femtosecond two-color electric field envelope. The corresponding THz emission profile appears to be strongly dependent on the experimental conditions. According to the models, a critical parameter for THz generation from two-color air plasma is the filament length L_f [9]. This length can be controlled by the characteristics of the pump pulse (duration, wavelength, energy) and the focusing strength, generally described by the numerical aperture $NA = R/f$, where R is the radius of the pump beam (measured at $1/e^2$ of the maximum beam intensity) before focusing and f the focal length of the focusing lens.

As the ω and 2ω pulses propagate along the filament, their relative phase changes, and we can define the dephasing length as $L_d = \lambda/[2(n_\omega - n_{2\omega})]$, where $\lambda = 800\ \ nm$ and $n_{\omega,2\omega}$ is the refractive index of the plasma filament at ω and 2ω, respectively. Because of this dephasing effect, maximum THz generation is expected for plasma filaments with length L_d about to 22-25 mm at 800 nm [9]. For long filaments (L_f in the order or longer than L_d), emission is conical across all THz frequencies, the higher the frequency, the smaller the aperture angle of the cone [10-12]. This has been recently clearly confirmed experimentally by Rasmussen *et al.* across the 1-15 THz range [13]. For short filaments ($L_f < L_d$), there is a limited effect of the dephasing between the two-color pulses and thus a limited oscillation of the microscopic current amplitude and polarity within the filament. As a result, the far-field THz radiation is less affected by the interference between the waves emitted from the local THz source distributed along the filament. In that case, THz emission is expected to show an unimodal (flat-top) beam at low frequencies and a conical one at higher frequencies [14,15]. This has been clearly demonstrated theoretically in Ref. 10, but experimental evidence is difficult to achieve since it requires proper detection to clearly differentiate the shape of the THz beam below and above 4 THz.

In this paper, we investigated the transition from unimodal to conical THz emission from two-color air plasma (the situation corresponding to $L_f < L_d$). For this purpose, we used four different experimental setups (THz camera, electro-optic sampling (EOS) in ZnTe and GaP crystals, air-biased coherent detection (ABCD) technique) to properly determine the THz beam shape as a function of the frequency from 0.2 up to 17.5 THz. We paid special attention to experimental artifacts that can mask on-axis THz emission, such as photo-excited losses in silicon wafers and the influence of the hole drilled in the center of the last mirror used to reflect the THz beam, and transmit the laser probe beam onto the detector. As a result, we determined that the THz beam exhibits a unimodal beam pattern below 4 THz and a conical beam pattern above 6 THz.

2 EXPERIMENTAL SETUPS

Investigating the frequency-resolved characterization of broadband THz beam generated by two-color air plasma is challenging since the spectral content of the corresponding THz ultrashort pulses spans nearly above two decades, typically from 0.1 to 100 THz. It is therefore almost impossible to use a single detection system to fully cover this ultra-wide spectral range. For this reason, we employed a set of four different experimental setups to properly characterize the far-field THz emission.

A commercially available THz camera (section 2.1) is usually mainly sensitive to high THz frequencies (> 4 THz). It is simple to use and provides a direct transverse two-dimensional (2D) image of the THz beam without any spectral information. 2D electro-optic sampling (2DEOS) in ZnTe crystal (section 2.2) is a very convenient method to record the time-resolved 2D profile of the THz electric field from 0.2 to 2 THz. This coherent detection provides a real-time image of the THz electric field including polarity information across the transverse profile of the THz beam. One-dimensional EOS (1DEOS) using balanced detection in a thin GaP crystal (section 2.3) can provide the global spectral content of the THz beam typically from 0.2 to 8 THz, limited by the spectral bandwidth of the crystal. We also used ABCD system (section 2.4) to extend the spectral detection to higher frequencies, even though this latter method presents reduced sensitivity below 4 THz.

2.1 Detection with an incoherent THz camera

For all setups presented in this paper (sections 2.1 to 2.4), the experimental conditions for THz generation are similar. An infrared femtosecond laser pulse (50 fs full width at half maximum, 800 nm, 1.5 mJ, R = 7 mm beam radius measured at $1/e^2$ of the maximum beam intensity, 1 kHz repetition rate) is focused in air by a plano-convex lens L1 with a focal length f of 300 mm (Fig. 1a). After passing through a beta barium borate (BBO) crystal for second harmonic generation, the resulting intense two-color laser pulse can produce a filament in air, whose length depends on the numerical aperture $NA = R/f = 0.023$ and the characteristics of the pump pulse (wavelength, energy, duration). In our case, the length of the plasma filament is estimated to $L_f = 5 \pm 1 \ \ mm$, as shown in Fig. 1a. This filament is more than 4 times shorter than L_d described in the introduction. Consequently, as explained in the introduction, we can expect that, under these experimental conditions, THz emission will exhibit a unimodal (flat-top) beam below 3-4 THz range and a conical one for higher frequencies.

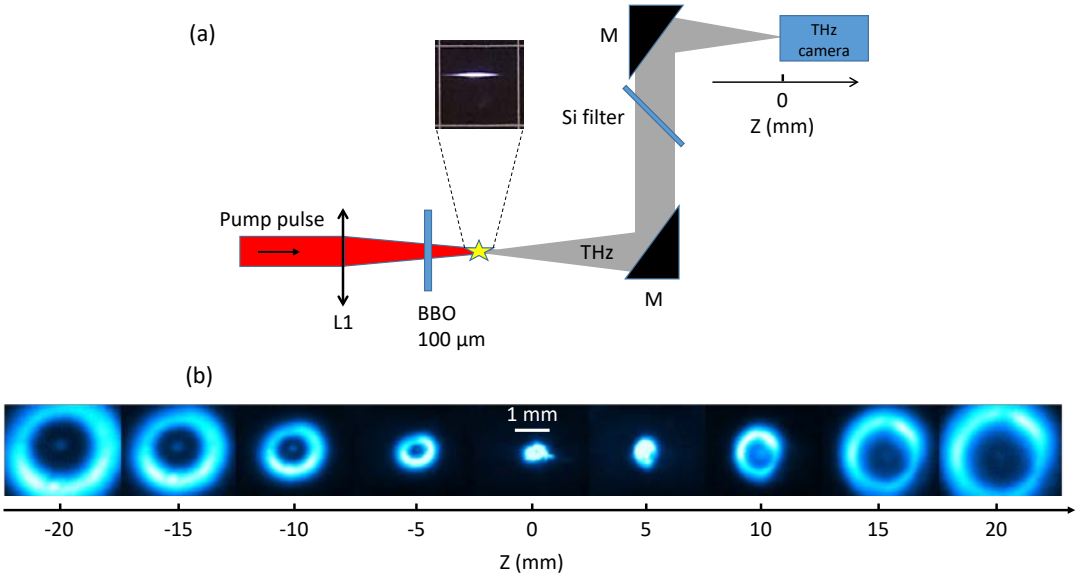

Fig. 1

THz radiation is collimated by an off-axis parabolic mirror M (f = 150 mm) and then focused onto a THz camera (RIGI from Swiss Terahertz, uncooled FPA 160x120 microbolometers, 25 µm pixel size) by a

second off-axis parabolic mirror M (f = 150 mm), after passing through a 1 mm-thick high-resistivity float zone silicon wafer, placed at Brewster angle, to filter out the remaining intense laser pump light. With this configuration, we carefully checked that the insertion of a high-density polyethylene (HDPE) window in front of the silicon wafer does not change the THz beam imaging, demonstrating that the detection is not affected by the photo-induced carriers in the silicon filter [16,17]. The THz camera is also more sensitive at high THz frequencies (> 4 THz). Consequently, THz imaging with this setup will not reflect properly the THz beam intensity below 4 THz. Figure 1b will be presented and discussed in section 3.

2.2 Detection with coherent 2DEOS in ZnTe crystal

The second detection system uses 2DEOS to measure the time-dependent spatial distribution of the THz electric field [15]. To effectively filter out the intense laser pump pulse, we employed a combination of a ceramic (96% Al_2O_3, 1 mm-thick) and a silicon (1 mm-thick) wafers (Fig. 2a). This setup ensures that the THz beam remains unaffected by photo-excited charge carriers while passing through the silicon wafer [16,17]. The THz beam is then sent into a large aperture (20 mm diameter), 1-mm-thick, ⟨110⟩ ZnTe crystal, positioned 60 mm behind the center of the plasma filament.

Using 2DEOS with a time-delayed femtosecond laser probe pulse, we map the distribution of the THz electric field onto the spatial profile of the laser probe beam (horizontally-polarized). The intensity of this latter is detected by a 256×256 pixels complementary metal oxide semiconductor (CMOS) camera, after passing through the analyzer AN (perpendicularly-oriented towards the probe beam polarization) and the objective lens L2 (f = 50 mm). For a given time delay between the THz and the probe pulses, the system captures a 2D image at 800 nm, representing the THz electric field distribution (Fig. 2b, Left). This image is acquired at a rate of 500 Hz, synchronized with the laser repetition rate.

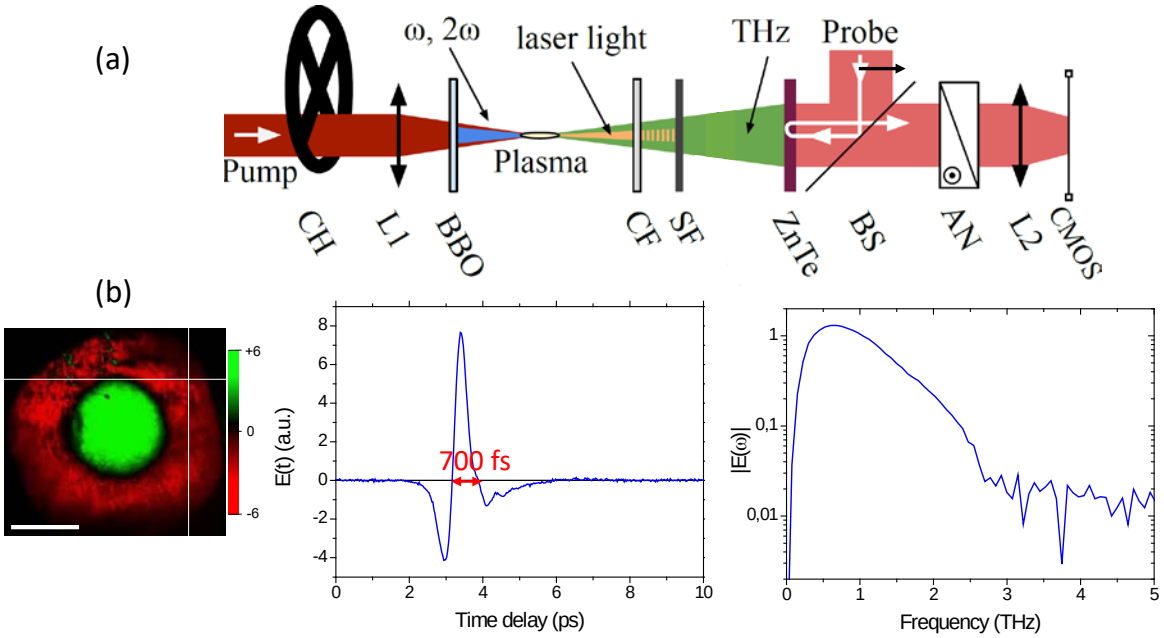

Fig. 2

For data analysis, each pixel in the stack of CMOS images provides the temporal evolution of the THz electric field at that position (Fig. 2b, Center). The Fourier transform of this temporal data yields the

frequency-resolved THz amplitude and phase at each pixel (Fig. 2b, Right). By performing this process across all the pixels of the CMOS images, we obtain the frequency-resolved 2D THz amplitude and phase distribution, limited by the spectral bandwidth and thickness of the ZnTe crystal and the filters. Based on experimental measurements, we determined that the effective spectral bandwidth, where the THz amplitude is at least 10 times higher than the noise level, ranges from 0.2 to 2.2 THz.

2.3 Aperture-scanning-assisted 1DEOS detection in GaP crystal

This detection is based on 1DEOS in GaP crystal and balanced detection. In this experiment, the THz beam travels through dry air, and the residual pump laser is blocked by a high-resistivity silicon wafer placed far away from the plasma to avoid any absorption of the THz beam. After passing through a set of four off-axis parabolic mirror M (f = 150 mm), the THz electric field is measured by a standard electro-optic detection using a 200 µm-thick ⟨110⟩ GaP crystal optically contacted onto a 3 mm-thick ⟨100⟩ GaP crystal (Fig. 3a). The probe pulse at 800 nm is transmitted by a hole (4 mm in diameter) drilled in the last parabolic mirror used to focus the THz pulse onto the GaP crystal. The time delay between the pump and THz pulses is adjusted with a delay line. To detect the spatial distribution of the THz beam, we used a sharp metallic circular aperture (7 mm in diameter) fixed on a motorized linear stage and sequentially translated horizontally across the entire THz beam (1 mm scan step). For each aperture-scanning step, a full THz waveform is recorded. After Fourier transform of the temporal data, we obtain the THz spectra and analyze the frequency-resolved THz beam profile along its horizontal axis.

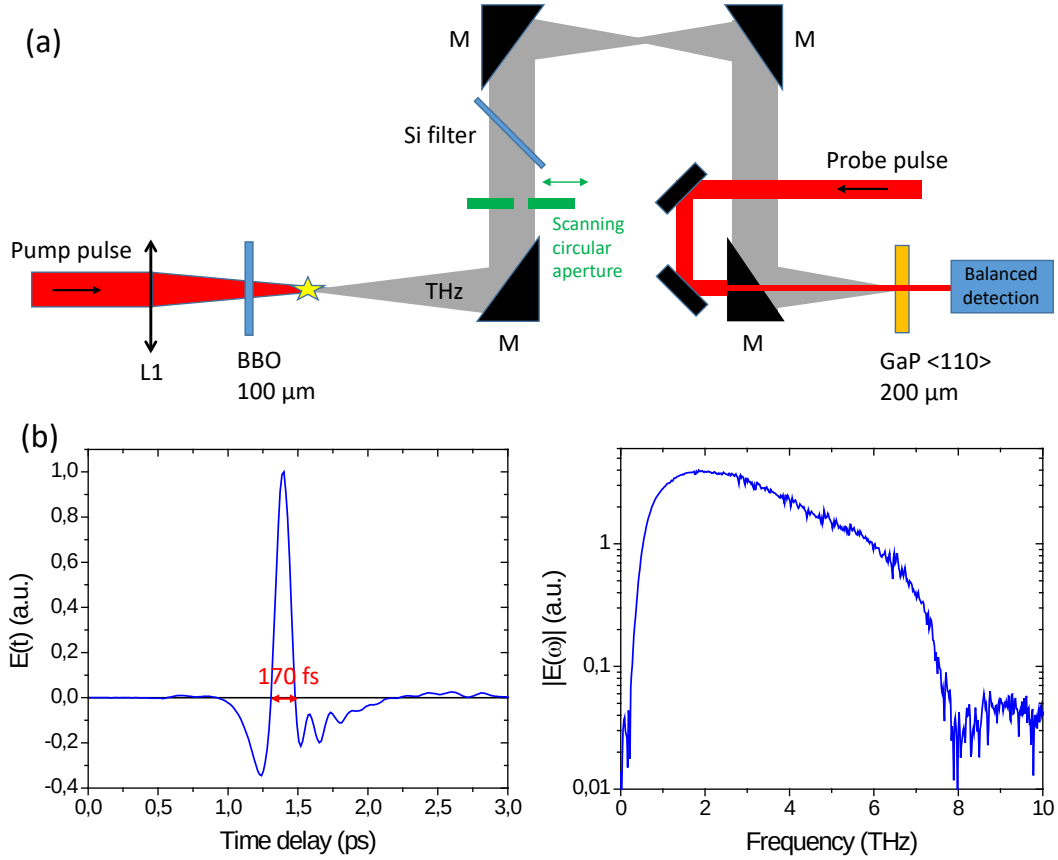

Fig. 3

Without any scanning aperture, a typical temporal evolution of the THz electric field generated with this setup is displayed in Fig. 3b (Left). The duration of the main positive THz transient is 170 fs. After Fourier transform of the temporal data, we determined that the effective spectral bandwidth, where the THz amplitude is at least 10 times higher than the noise level, ranges from 0.4 to 6.8 THz, limited by the acceptance bandwidth and the thickness of the GaP sampling crystal (Fig. 3b, Right).

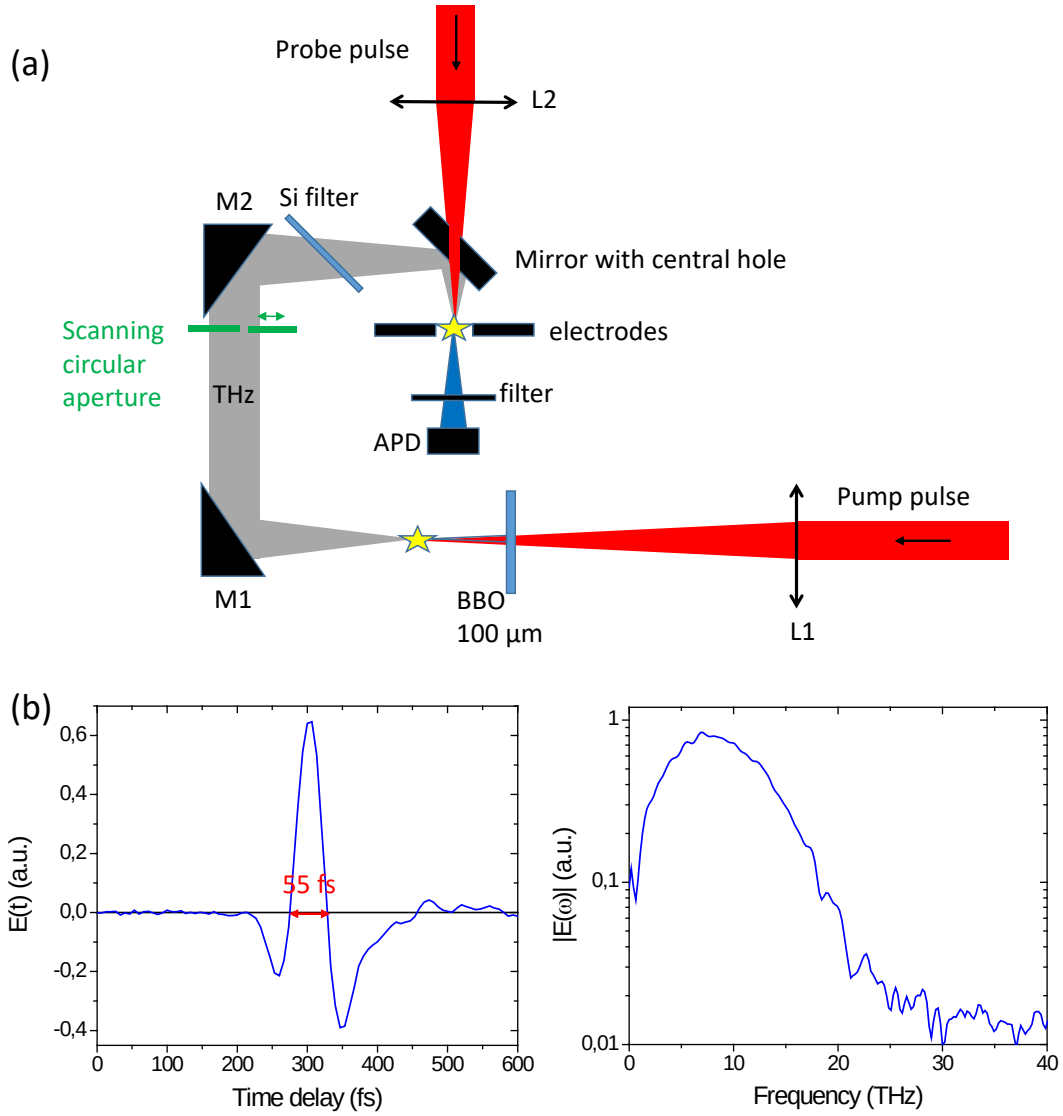

Fig. 4.

2.4 Aperture-scanning-assisted ABCD technique

This detection is based on the ABCD technique, widely used for air-photonics THz detection [17]. We used the commercial model ZAP-APD from Daheng Optics. Briefly, a probe femtosecond laser beam, after passing through a small hole (1 mm in diameter) drilled in the flat parabolic mirror reflecting the THz beam, is focused in air to ignite a plasma. When the THz pulse is also focused into this plasma, second harmonic generation can occur through the THz field-induced second harmonic (TFISH) process (Fig. 4a). Using heterodyned detection composed of two high voltage electrodes, a variable delay stage, and an avalanche

photodiode (APD), the measured second harmonic signal is proportional to the transient THz electric field. The residual pump laser is blocked by a high-resistivity silicon wafer placed far away from the plasma to avoid any absorption of the THz beam. To detect the spatial distribution of the THz beam, we used a circular aperture (7 mm in diameter) fixed on a motorized linear stage and sequentially translated horizontally across the entire THz beam (1 mm scan step). For each aperture-scanning step, a full THz waveform was recorded.

Without any scanning aperture, a typical temporal evolution of the THz electric field generated with this setup is displayed in Fig. 4a (Left). The duration of the main positive THz transient is 55 fs. After Fourier transform of the temporal data, we estimated that the effective spectral bandwidth, where the THz amplitude is at least 10 times higher than the noise level, ranges from 1.0 to 17.5 THz, limited by the laser pulse duration and potential misalignment between the laser probe beam and the THz beam (Fig. 4b, Right).

3 EXPERIMENTAL RESULTS AND DISCUSSION

In this section, we present the results obtained with the four experimental setups described earlier, followed by a brief conclusion at the end of each sub-section. A comprehensive summary and analysis of all the data will be presented in section 4.

3.1 Detection with an incoherent THz camera

Fig. 1b shows the evolution of the THz beam along the propagation axis Z, focused by the mirror M, where Z=0 corresponding to the beam-waist position (see Fig. 1a). Consistent with previous studies [9-12], THz imaging reveals a distinct conical emission pattern before and after the beam-waist, converging into a solid near-Gaussian beam distribution close to Z=0. At the focus, the spatial mode of the beam deviates from perfect Gaussian shape, which can pose challenges in THz-TDS experiments that require homogeneous sample excitation. Based on these images, the half-opening angle (HOA) of the THz beam is estimated to be between 5° and 6°. This divergence angle represents an average over frequencies spanning from low THz frequency to mid-infrared, due to the broad spectral response of the camera. Additionally, the THz far-field beam profile exhibits slight asymmetry, attributed to spatial walk-off effects between the fundamental and second harmonic in the BBO crystal [13]. Furthermore, a bright spot is observed at the center of the THz beam, particularly evident before and after the focus plane. This phenomenon is attributed to the Poisson or Fresnel spot predicted by diffraction theory when light encounters a circular obstacle, such as the off-axis parabolic mirrors used in our setup [19].

From these initial findings, we conclude that the far-field THz emission from two-color air plasma, observed with a standard THz camera, conforms to a conical shape as documented in previous studies [10-13]. However, due to the broad spectral response of the camera without specific filtering, determining the spectral dependence of this predominant bright ring emission is challenging. We can only infer that within the spectral sensitivity of the THz camera (from 1 to 18 THz), any contribution from a unimodal THz emission is not dominant.

3.2 Detection with coherent 2D electro-optic sampling (2DEOS) in ZnTe crystal

In this section, we discuss the conclusions drawn from a previously published study in 2020, focusing on the characterization of conical versus Gaussian THz emission from two-color laser-induced air plasma filaments [17]. This study did not investigate the frequency-dependence of THz emission but rather explored the influence of experimental filtering conditions.

When an alumina wafer is positioned before the commonly used silicon wafer, the THz emission exhibits a Gaussian-like profile for frequencies ranging from 0.2 and 2.5 THz (Fig. 2a). The width of this profile slightly decreases with increasing frequencies, consistent with previous findings that demonstrate unimodal angular distribution of THz emission at lower frequencies for short filament lengths [14,15]. This observation is illustrated in Fig. 5a, including two insets showing the 2D spatial distributions of THz electric field amplitude at 0.37 THz and 1.05 THz, both highlighting the unimodal THz profiles when the ceramic filter is used first.

Conversely, when the silicon filter is placed first, a central dark region becomes evident for frequencies above 0.5 THz (Fig. 5b). The HOA of this central dark region measures approximately 3.5° at 0.5 THz, decreasing to below 3.0° at 2.5 THz. The insets also depict 2D spatial distributions of THz electric field amplitude at different frequencies. At 1.05 THz (dotted white line in Fig. 5b), a clear conical THz profile is observed. Below 0.5 THz (dotted white line at 0.37 THz), a central peak within a bright ring is attributed to a diffraction pattern. Therefore, the silicon filter acts as a reflective or absorbing material for THz radiation in this region due to the presence of photocarriers induced by the remaining pump laser light, resulting in the observed diffraction pattern below 0.5 THz. We believe that the conical THz emission observed beyond 0.5 THz in our experimental conditions is influenced by the presence of the silicon filter. It is important to distinguish this from the conical emission typically expected at higher THz frequencies (> 4 THz).

From these findings, we conclude that below 2.5 THz, the THz beam exhibits an almost unimodal Gaussian spatial distribution when preceded by a large bandgap ceramic filter before the silicon wafer. This highlights the critical importance of the positioning of the silicon wafer: it should be either preceded by another filter or placed sufficiently far away from the filament to prevent photo-excited losses and consequent undesired on-axis THz absorption.

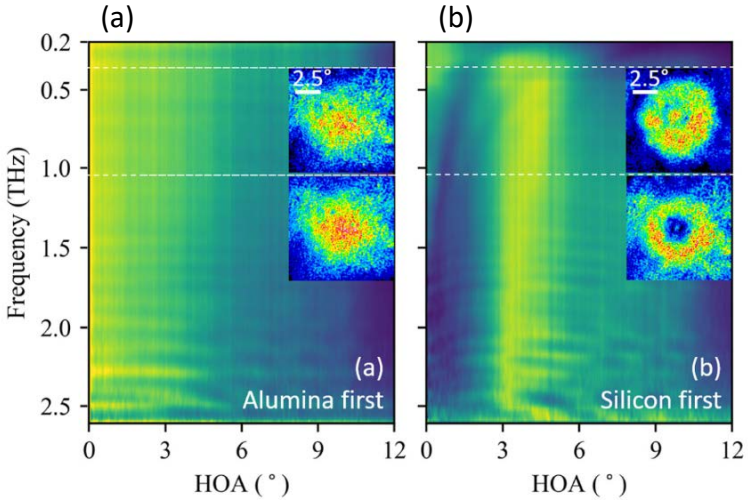

Fig. 5.

3.3 Aperture-scanning-assisted 1DEOS in GaP crystal

In this experiment, a circular aperture is scanned horizontally across the THz beam, with a 1 mm scan step (Fig. 3a). Additionally, the laser probe pulse is transmitted through a hole (4 mm in diameter) drilled in the last parabolic mirror used to focus the THz pulse onto the GaP crystal. Fig. 6a depicts the variation of the THz amplitude with frequency and pinhole position. Despite slight asymmetry attributed to optical misalignment, there is a noticeable reduction in size of the THz beam size with increasing THz frequency. This trend aligns with previous assessments indicating higher frequencies are distributed within smaller aperture angles [10-12]. Moreover, a central hole is evident in the THz beam across all frequencies. It has been confirmed that the insertion of a HDPE window in front of the silicon wafer does not influence this central hole, indicating it is not caused by photo-induced carriers in the silicon filter [16,17].

From Fig. 6a, we can extract the integrated spectra for different spectral windows, illustrated in Fig. 6b. The plot marked with black squares represents integration over the total THz spectral range. The red circles denote integration between 0 and 4 THz, while the blue triangles represent the spectral range above 4 THz. In all three spectra, the reduction in THz radiation at the center of the beam is clearly observable.

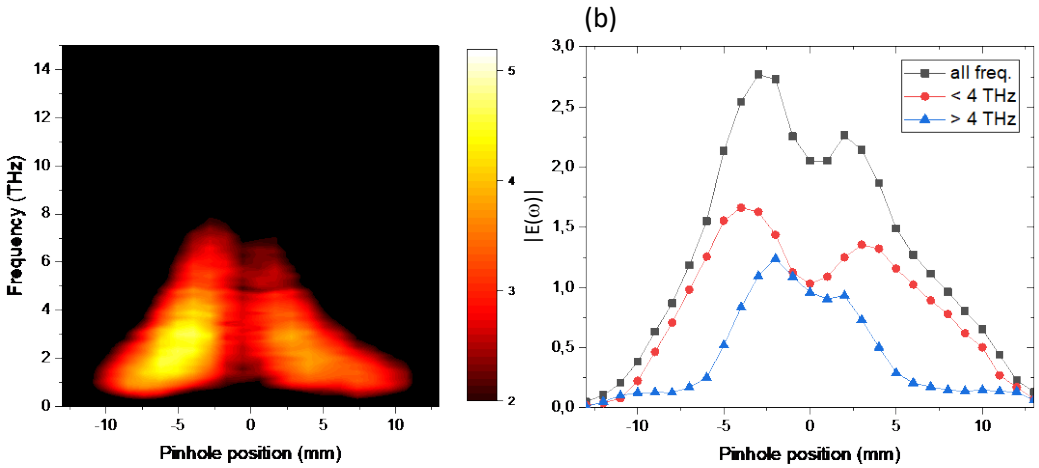

Fig. 6.

In a modified experiment aiming at investigating the influence of the central hole drilled in the last parabolic mirror (not shown in Fig. 3a), we replaced this mirror with a focusing lens (f = 200 mm, 50 mm in diameter) followed by an ITO (Indium Tin Oxide) plate that reflects the THz beam while transmitting the laser probe beam. This setup ensures that the central part of the THz beam incident on the GaP crystal remains unaffected during focusing. Fig. 7a and Fig. 7b clearly show that after replacing the parabolic drilled mirror with the lens and ITO plate setup, the central black hole in the THz beam has disappeared, and the THz beam exhibits a unimodal emission at all frequencies. This experimental change demonstrates the significant impact of the drilled parabolic mirror, which can strongly alter the THz beam profile by obstructing a substantial portion of the beam. Based on the 20 mm diameter of the THz beam before the drilled mirror, from Fig. 7a, we estimated that the THz power intercepted by the 45°-oriented hole with a diameter of 4 mm in the center of the THz beam corresponds to 10% of the total THz power, which is consistent with the ratio between the hole and the THz beam areas. This power amount is not negligible

if this detection is used for calibrating the THz electric field strength.

From this experiment, two conclusions can be drawn. First, in addition to potential absorption losses caused by the silicon wafer, the use of mirrors with a central hole introduces an experimental artifact in the characterization of THz emission from two-color air plasma. Second, within the effective spectral bandwidth defined for this experiment (0.4 to 6.8 THz, section 2.3), the THz emission exhibits a unimodal beam pattern.

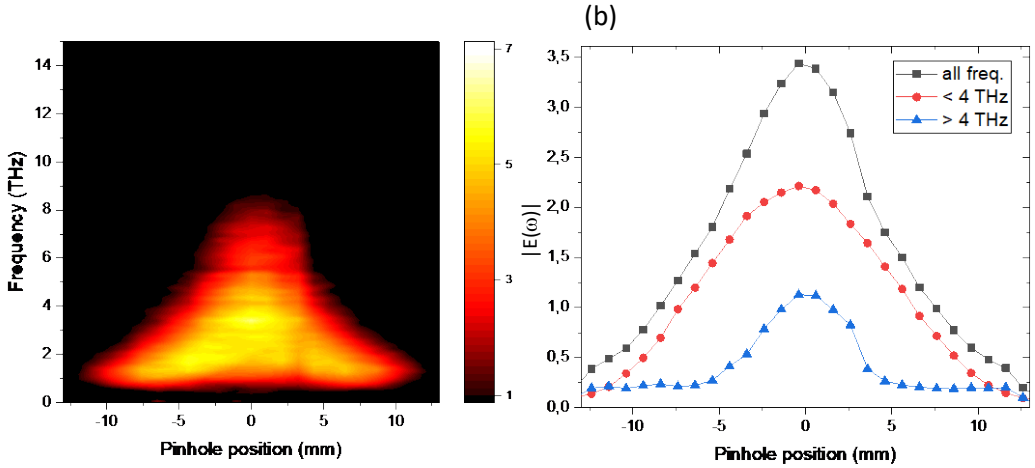

Fig. 7.

3.4 Aperture-scanning-assisted ABCD technique

Building on the findings from sections 3.3 (Figs. 6 and 7), adjustments were made to the ABCD setup to prevent THz beam reflection onto the drilled mirror prior to reaching the electrodes. This modification involved placing an ITO plate over the drilled mirror surface to ensure full reflection of the THz beam, while allowing transmission of the probe beam through the combination of the drilled mirror and the ITO plate. Additionally, we added a thin (2 mm-thick) PEHD filter before the silicon wafer to prevent any photo-excited losses of THz emission. This filter was thin enough to avoid significant spectral bandwidth attenuation up to 15 THz.

Fig. 8a illustrates the evolution of the THz amplitude as a function of frequency and pinhole position. Above 6 THz, clear conical THz emission is observed, consistent with the THz images presented in Fig. 1b. The conical emission is frequency-resolved, with $HOA \simeq 15°$ at 6 THz (corresponding to a cone radius of about 7 mm, collimated by a parabolic mirror with a 150 mm focal length), decreasing to $HOA \simeq 7°$ at 15 THz. Figure 8b presents integrated spectra for various spectral windows. Conical THz emission is visible for both total spectral integration and integration above 4 THz, even if the region between 4 and 6 THz can be considered as a transition from unimodal to conical emission. As explained in the introduction, the frequency of this transition is strongly governed by the plasma length [9,10].

Another prominent feature observed in Fig. 8a is the presence of unimodal emission between 2 and 4 THz, clearly depicted in Fig. 8b (red plots, spectral integration below 4 THz). Below 2 THz, the THz signal amplitude notably diminishes due to reduced sensitivity of the ABCD technique in this frequency range. Figure 8c further explores the THz spectra at different pinhole positions. At the center of the THz beam (black curve), the spectrum peaks around 4 THz, corresponding to the spectral content of the

unimodal emission. At a position associated with conical emission (red curve), the THz spectrum is broader with a peak around 8 THz. Outside the conical emission region (blue curve), the THz beam shows significant attenuation at higher frequencies, with most spectral content below 5 THz.

In summary, this sub-section underscores the effectiveness of the ABCD technique in spectrally resolving THz beams emitted from two-color air plasma. Within the effective spectral bandwidth defined for this experiment (1 to 17.5 THz, section 2.4), simultaneous observation of unimodal THz emission below 4 THz and conical emission above 6 THz is achieved, consistent with theoretical predictions in Refs. 14 and 15. However, due to sensitivity limitations below 1 THz, detailed characterization of THz emission at these lower frequencies was not feasible with this setup. We can also compare and discuss Figs. 7a and 8a, obtained with balanced detection in GaP crystal and ABCD technique, respectively. Both plots should show the same features since the data were obtained in the same experimental conditions, i.e. without any artifacts such as the influences of the silicon wafer and the drilled mirror. However, surprisingly, Fig. 7a does not exhibit the conical emission beyond 6 THz. This can be explained by the limited spectral bandwidth of the GaP detection, previously estimated to be between 0.4 and 6.8 THz. Also, the amplitude of the THz spectrum at 6 THz in the case of GaP detection is about half of the spectrum peak amplitude, whereas it corresponds to the maximum of the THz amplitude in case of the ABCD technique. These results emphasize the importance of experimental configuration and technique selection in accurately characterizing the spectral and spatial properties of THz radiation emitted by laser-induced air plasmas.

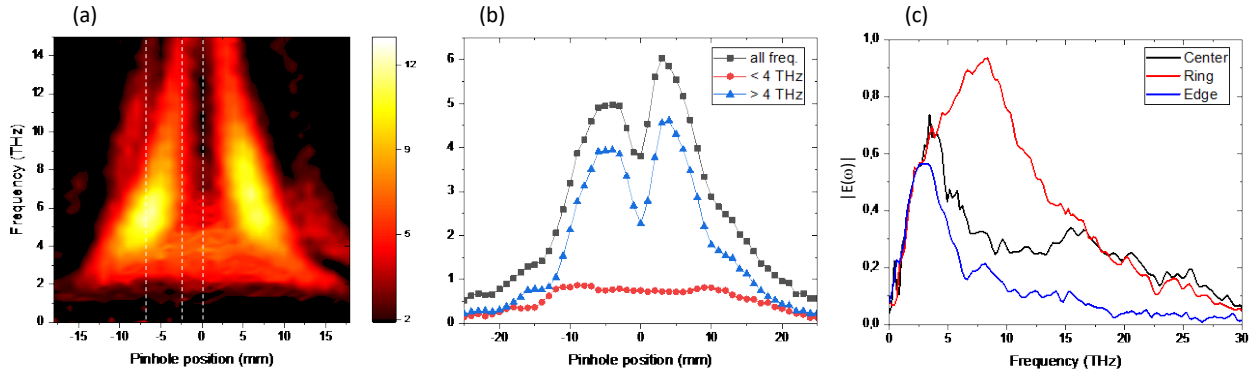

Fig. 8.

4 CONCLUSION

Based on a comprehensive investigation using four different experimental setups, we explored the spectral dependence of far-field THz emission from a two-color laser-induced air plasma filament. Under our experimental conditions (filament length L_f shorter than the dephasing length L_d between the two-color pulses), we draw the following main findings and conclusions from each experimental approach.

In the experiment using a standard THz camera, we observed a clear conical THz emission, consistent with previous studies. This method did not detect any potential unimodal THz emission due to its incoherent detection nature, primarily sensitive to high THz frequencies (> 4 THz). To enhance the detection of the unimodal component of the THz emission, one should incorporate a low-pass THz filter (cut-off frequency < 4 THz) in front of the camera.

Using coherent 2DEOS in a ZnTe crystal revealed an almost unimodal Gaussian spatial distribution

of THz emission below 2.5 THz. We emphasized the importance of minimizing photo-excited losses in silicon to mitigate severe on-axis THz absorption.

The aperture-scanning-assisted 1DEOS in GaP crystal exposed an artifact arising from the use of mirrors with a central hole, affecting the central part of the THz beam. After correcting this artifact, the THz beam exhibited a unimodal pattern within the effective spectral bandwidth of the experiment (0.4 to 6.8 THz).

Finally, using aperture-scanning-assisted ABCD technique with an ITO plate modification to reject the previous artifact, we clearly distinguished unimodal THz emission below 4 THz and conical emission above 6 THz. These results are consistent with numerical simulations based on the unidirectional pulse propagation equation for short filament lengths ($L_f < L_d$) [8,14,15].

In conclusion, each experimental configuration provided valuable insights into the spectral characteristics of THz emission from two-color laser-induced air plasma. This study highlights the critical role of experimental setup and artifact mitigation for accurate characterization of THz beams. Future perspectives include investigating the evolution of THz emission with various filament lengths to further enhance experimental understanding and validate available theoretical models.

Conflict of interest

The authors declare that they have no competing interests to report.

Funding

The work was funded by Quantum Matter Bordeaux, a synergy program of Bordeaux University involving Chemistry, Physics, Mathematics, Applied and Computer Sciences, and by the HIRAKU-Global Program, which is funded by MEXT's "Strategic Professional Development Program for Young Researchers" and Research Clusters program of Tokushima University (2201001).

Data availability statement

The data associated with this study is available upon request. Please contact the corresponding author to request access to the data.

Author contribution statement

All authors contributed equally to this work.

References

[1] D. J. Cook, and R. M. Hochstrasser, "Intense terahertz pulses by four-wave rectification in air", Optics Letters, **25**(16), 1210-2, (2000).

[2] M. Kress, T. Löffler, S. Eden, M. Thomson, and H. G. Roskos, "Terahertz-pulse generation by photoionization of air with laser pulses composed of both fundamental and second-harmonic waves", Optics Letters, **29(10)**, 1120-1122, (2004).

[3] H. Zhong, N. Karpowicz, and X.-C. Zhang, "Terahertz emission profile from laser-induced air plasma", Applied Physics Letters, **88**, 261103, (2006).

[4] H. G. Roskos, M. D. Thomson, M. Kreß, and T. Löffler, "Broadband THz emission from gas plasmas induced by femtosecond optical pulses: From fundamentals to applications", Laser & Photonics Reviews, **1**(4), 349-368, (2007).

[5] T. I. Oh, Y. S. You, N. Jhajj, E. W. Rosenthal, H. M. Milchberg, and K.Y. Kim, "Intense terahertz generation in two-color laser filamentation: energy scaling with terawatt laser systems", New Journal of Physics, **15**(7), 075002, (2013).
[6] J. Zhao, W. Liu, S. Li, D. Lu, Y. Zhang, Y. Peng, Y. Zhu, and S. Zhuang, "Clue to a thorough understanding of terahertz pulse generation by femtosecond laser filamentation," Photonics Research, **6**, 296-306, (2018).
[7] A. Gorodetsky, A. D. Koulouklidis, M. Massaouti, and S. Tzortzakis, "Physics of the conical broadband terahertz emission from two-color laser-induced plasma filaments," Physical Review A, **89**(3), 033838, (2014).
[8] L. Bergé, S. Skupin, C. Köhler, I. Babushkin, and J. Herrmann, "3D Numerical Simulations of THz Generation by Two-Color Laser Filaments", Physical Review Letters, **110**, 073901, (2013).
[9] Y. S. You, T. I. Oh, and K. Y. Kim, "Off-Axis Phase-Matched Terahertz Emission from Two-Color Laser-Induced Plasma Filaments," Physical Review Letters, **109**(18), 183902, (2012).
[10] A. A. Ushakov, P. A. Chizhov, V. A. Andreeva, N. A. Panov, D. E. Shipilo, M. Matoba, N. Nemoto, N. Kanda, K. Konishi, V. V. Bukin, M. Kuwata-Gonokami, O. G. Kosareva, S. V. Garnov, and A. B. Savel'ev, "Ring and unimodal angular-frequency distribution of THz emission from two-color femtosecond plasma spark," Optics Express **26**(14), 18202 (2018).
[11] P. Klarskov, A. C. Strikwerda, K. Iwaszczuk, and P. U. Jepsen, "Experimental three-dimensional beam profiling and modeling of a terahertz beam generated from a two-color air plasma," New Journal of Physics **15**(7), 075012, (2013).
[12] I. A. Nikolaeva, N. R. Vrublevskaya, G. E. Rizaev, D. V. Pushkarev, D. V. Mokrousova, D. E. Shipilo, N. A. Panov, L. V. Seleznev, A. A. Ionin, O. G. Kosareva, and A. B. Savel'ev, "Terahertz ring beam independent on ω–2ω phase offset in the course of two-color femtosecond filamentation," Applied Physics Letters, **124**(5), 051105, (2024).
[13] M. Rasmussen, O. Nagy, S. Skupin, A. Stathopulos, L. Berge, P. Jepsen, and B. Zhou, "Frequency-resolved characterization of broadband two-color air-plasma terahertz beam profiles," Optics Express, **31**(6), 9287, (2023).
[14] V. Blank, M. D. Thomson, and H. G. Roskos, "Spatio-spectral characteristics of ultra-broadband THz emission from two-colour photo-excited gas plasmas and their impact for nonlinear spectroscopy," New Journal of Physics, **15**(7), 075023 (2013).
[15] V. A. Andreeva, O. G. Kosareva, N. A. Panov, D. E. Shipilo, P. M. Solyankin, M. N. Esaulkov, P. González de Alaiza Martínez, A. P. Shkurinov, V. A. Makarov, L. Bergé, and S. L. Chin, "Ultrabroad Terahertz Spectrum Generation from an Air-Based Filament Plasma," Physical Review Letters **116**(6), 063902, (2016).
[16] J. Degert, M. Tondusson, V. Freysz, E. Abraham, S. Kumar, and E. Freysz, "Ultrafast, broadband and tunable terahertz reflector and neutral density filter based on high resistivity silicon," Optics Express, **30**(11), 18995-19004, (2022).
[17] C. B. Sørensen, L. Guiramand, J. Degert, M. Tondusson, E. Skovsen, E. Freysz, and E. Abraham, "Conical versus Gaussian terahertz emission from two-color laser-induced air plasma filaments," Optics Letters, **45**(7), 2132-2135, (2020).
[18] E. Prost, V. Loriot, E. Constant, I. Compagnon, L. Bergé, F. Lépine, and S. Skupin, "Air-photonics based terahertz source and detection system," The European Physical Journal – Special Topics, https://doi.org/10.1140/epjs/s11734-022-00748-7, (2022).

[19] E. Hecht, Optics (Pearson, 5th edition, 2017), page 516.

Figure captions

Fig. 1. (a) Experimental setup: detection with a THz camera. L: plano-convex lens (f = 300 mm) ; M: off-axis parabolic mirror (f = 150 mm). Inset: picture of the plasma filament (the size of the square is 1x1 cm^2). (b) Evolution of the THz beam along the Z-axis, as defined in (a).

Fig. 2. Coherent 2D electro-optic sampling setup using ZnTe detection crystal. (a) Experiment. CH: optical chopper for dynamic subtraction ; L1: plano-convex lens (f = 300 mm) ; CF: ceramic filter ; SF: silicon filter ; BS: beamsplitter ; AN: analyzer ; L2: objective lens (f = 50 mm). (b) Left: 2D transverse profile of the THz electric field for a given time delay between the THz and probe pulses (scale: the white bar is 5 mm long) ; Center: temporal evolution of the THz electric field at the position corresponding to the intersection of the white lines (left image) ; Right: corresponding amplitude of THz spectrum.

Fig. 3. (a) Aperture-scanning-assisted balanced detection in GaP crystal. (a) Experiment. L1: plano-convex lens (f = 300 mm) ; M: off-axis parabolic mirror (f = 150 mm, diameter = 40 mm) ; (b) Left: temporal evolution of the THz electric field ; Right: corresponding amplitude of THz spectrum.

Fig. 4. Aperture-scanning-assisted balanced detection with ABCD system. (a) Experiment. L1: plano-convex lens (f = 300 mm) ; L2: plano-convex lens (f = 200 mm) ; M1: off-axis parabolic mirror (f = 100 mm, diameter = 50 mm) ; M2: off-axis parabolic mirror (f = 150 mm, diameter = 50 mm). (b) Left: temporal evolution of the THz electric field ; Right: corresponding amplitude of THz spectrum.

Fig. 5. Coherent 2DEOS in ZnTe crystal. Evolution of THz amplitude as a function of frequency and HOA. (a) Alumina first. (b) Silicon first. Yellow color indicates a higher THz amplitude. Insets: 2D spatial distributions of the THz electric field at 0.37 THz and 1.05 THz (from Ref. 17).

Fig. 6. Aperture-scanning-assisted balanced detection in GaP crystal. The laser probe pulse is transmitted by a hole (4 mm in diameter) drilled in the last parabolic mirror used to focus the THz pulse onto the GaP crystal. (a) Evolution of THz amplitude as a function of frequency and pinhole position. (b) Amplitude of the spectra integrated for different spectral windows.

Fig. 7. Aperture-scanning-assisted balanced detection in GaP crystal. The parabolic mirror with a hole has been replaced by a lens followed by an ITO plate. (a) Evolution of THz amplitude as a function of frequency and pinhole position. (b) Amplitude of the spectra integrated for different spectral windows.

Fig. 8. Aperture-scanning-assisted ABCD technique. The drilled mirror has been covered by an ITO plate. (a) Evolution of THz amplitude as a function of frequency and pinhole position. (b) Integrated spectra for different spectral bandwidths. (c) Amplitude of the spectra at three different positions of the pinhole, as indicated by the dashed line in (a). “Center” refers to 0 mm (spectrum at the center of the THz beam), “Ring” refers to -2.5 mm (spectrum along the emission cone emitted at high frequency, above 12 THz), “Edge” refers to -7 mm (spectrum at the edge of the emission cone).